Round Robin test for Total Reflection X-Ray Fluorescence Analysis using preselected and well characterized samples

Rainer Unterumsberger, Burkhard Beckhoff
Physikalisch-Technische Bundesanstalt, Abbestr. 2-12, 10587 Berlin, Germany

Armin Gross, Hagen Stosnach
Bruker Nano GmbH, Am Studio 2D, 12489 Berlin, Germany

Sascha Nowak, Yannick P. Stenzel
MEET - Battery Research Center Office, Corrensstr. 46, 48149 Münster, Germany

Markus Krämer
AXO DRESDEN GmbH, Gasanstaltstr. 8b, 01237 Dresden, Germany

Alex von Bohlen
Leibniz-Institut für Analytische Wissenschaften - ISAS - e.V.,
Bunsen-Kirchhoff-Str. 11, 44139 Dortmund, Germany

Supporting Information

A   GIXRF measurement

Grazing incidence X-ray fluorescence (GIXRF) uses a small glancing angle for exciting samples to X-ray fluorescence. Typically, angles of approximately 0.1° are used to achieve insight into some special properties of materials and the distribution of elements near the surface. In most cases GIXRF is offered at Synchrotron facilities [1, 2] due to the excellent control of the beam geometry used for excitation.

Total reflection X-ray fluorescence can be described as measuring an EDXRF spectrum at a fixed glancing angle Θ_{TXRF}. The angle for the primary beam used for excitation to X-ray fluorescence should be below the critical angle of external total reflection of the X-rays used. Best condition can be achieved at about 70 % of the critical angle. The spectrum displays the intensity versus the energy of photons. GIXRF uses an angular scan of the primary beam at very small glancing angles. The signals of preselected energies are recorded along the angular scan. In a certain way TXRF is a single static view of one position of GIXRF containing all the energies detected.

On flat surfaces and for glancing angles below the critical angle of external total reflection, the interference of the incoming and reflected beam result in an X-ray standing wave (XSW) field [3]. The intensity distribution of the XSW field is very sensitive on a variation of the incident angle of the excitation radiation. It directly influences the emitted fluorescence line intensity of an element in a sample located at the surface, revealing information about the vertical distribution [4, 5] with respect to the sample surface. In Figure 1, simulations of Ni layers with several thicknesses on quartz glass substrates show the development of the XSW field intensity inside of the respective layers as a function of incident angle.

For thin films, the enhancement below the critical angle of total external reflection of the substrate can be up to a factor of about 4 (in this simulation at 0.1075° for an excitation energy of 17.44 keV). For particle-like distributions over a height region of 100 nm, a factor of about 2 over a larger range of incident angles below the critical angle of total external reflection arises. Above the critical angle, the XSW field collapses and the relative intensity becomes one. Surface roughness and the divergence of the incident beam averages out the sinuous behavior and can reduce the XSW field intensity [6, 7].

Figure 2a shows the experimentally determined XSW field intensity from a 50 ng µL droplet sample for an excitation energy of 10.5 keV, measured with monochromatized synchrotron radiation at the FCM beamline [8] in the PTB laboratory at BESSY II. There is no difference in the characteristic of the intensity as a function of the incident angle except for Ni, allowing for the assumption of one film, where all elements are mixed. The enhancement factor I_{XSW} below the critical angle of total external reflection is about 1.4 to 1.8 for the elements Ga, Sc and Mn, being in line with an assumed surface roughness of several 10 nm as a model parameter for the simulation of the respective XSW field intensity. Ni shows an even lower enhancement factor. This can be explained by an excitation radiation induced fluorescence radiation of instrumentation materials,
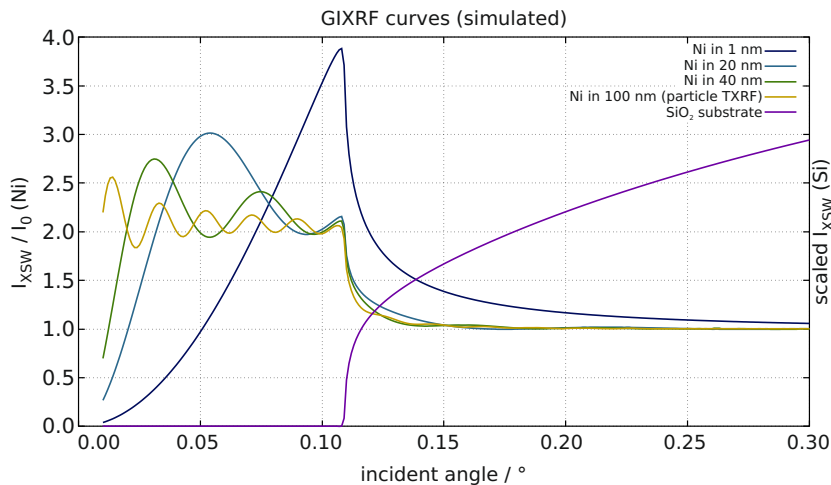
Figure 1: Simulation of the intensity distribution of the XSW field for Ni layers with several thicknesses at 17.44 keV incident photon energy. The intensity distribution of Si from the glass substrate was simulated for the same XSW field and shows the evanescent part above the critical angle of external total reflection. It has been upscaled for a better comparability.

reaching the X-ray detector by a second scattering process e.g. at the substrate, or alternatively by a direct substrate contamination. The Ni intensity as a function of the incident angle would then be a combination of the signal of the Ni from the droplet on the substrate surface and the excitation radiation induced fluorescence radiation of instrumentation materials, which is independent on the incident angle. For µL droplet samples, a GIXRF measurement at a position of the substrate without sample has been performed and shows a constant Ni background for all incident angles. This background measurement was used for a correction of the GIXRF measurement for Ni originated from the sample.

With current generation table-top TXRF instrumentation it is also possible to perform a GIXRF measurement for a qualitative validation of the curve shape and to ensure the optimal adjustment of the incident angle. In Figure 2b a table-top GIXRF measurement for a similar sample is shown. Here, the excitation energy is 17.44 keV (Mo-Kα) and the respective critical angle of total external reflection is about 0.1°. Comparison to the synchrotron-radiation-based GIXRF measurement shows similar development of the curves and illustrates the performance of the table-top instrumentation. Above the critical angle of total external reflection, the signal of the background is increasing rapidly in comparison to the fluorescence lines and can negatively affect the deconvolution. This can be seen most notably in the Sc count rate, where the run of the curve follows the substrate signal. The total measurement time of the table-top GIXRF measurement shown here was rather short with about 75 min, already suitable for a qualitative analysis of the sample.
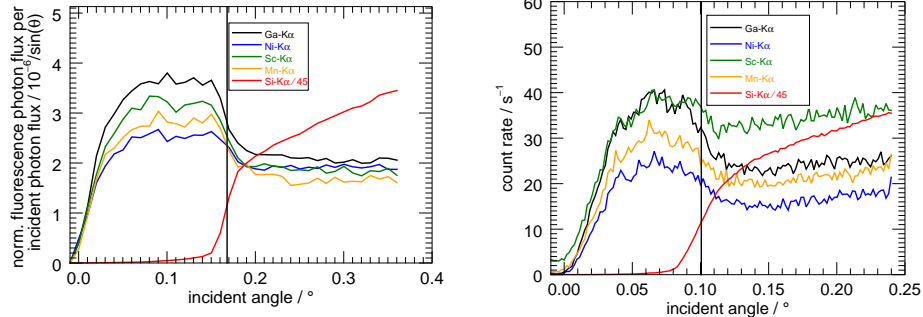
(a) Experimental determined, normalized fluorescence photon flux for Sc, Mn, Ni and Ga from a 50 ng µL droplet sample (excitation energy 10.5 keV). The normalized photon flux of the Si fluorescence from the substrate increases rapidly above the critical angle of total external reflection.

(b) GIXRF measurement with a table-top instrument. Measurement parameter: scanning range in steps: 4000 to 4750, step size: 5, measurement time per step: 30 s, total measurement time: 75 min.

Figure 2: GIXRF measurements with monochromatized synchrotron radiation (10.5 keV incident beam energy) and with table-top instrumentation (Mo-Kα X-ray tube excitation).

B   Lateral measurement

Based on the GIXRF measurement with monochromatized synchrotron radiation, the incident angle for the lateral measurement was chosen to be 0.1175°, which is well below the critical angle of total external reflection for SiO_2 at 10.5 keV (about 0.168°). For this incident angle, the experimentally determined enhancement factor I_{XSW} is 1.4 to 1.8, described in detail in section A. In order to use I_{XSW} for the quantification at every vertical lateral position of the sample, the assumption was made that the formation of the XSW field is similar at every vertical lateral position. This assumption has been experimentally verified for one of the samples.

The vertical size, particularly the full width at half maximum (FWHM) value of the incident beam with a Gaussian distribution, was about 100 µm and was experimental determined with a knife-edge scan [9, 10]. The size of the beam in the propagation direction is drastically increased from a horizontal beam size of about 270 µm to a footprint of about 130 mm because of the TXRF-conditions with an incident angle of 0.1175°. It is important to have a footprint of the incident beam larger than the sample area in this direction because it is essential for the absolute quantification to excite the whole material in propagation direction while doing a lateral scan of the sample in the vertical direction. Figure 3a shows the normalized fluorescence photon flux of the elements Ga, Ni, Mn and Sc from a 50 ng µL droplet sample as a function of the vertical position.

4
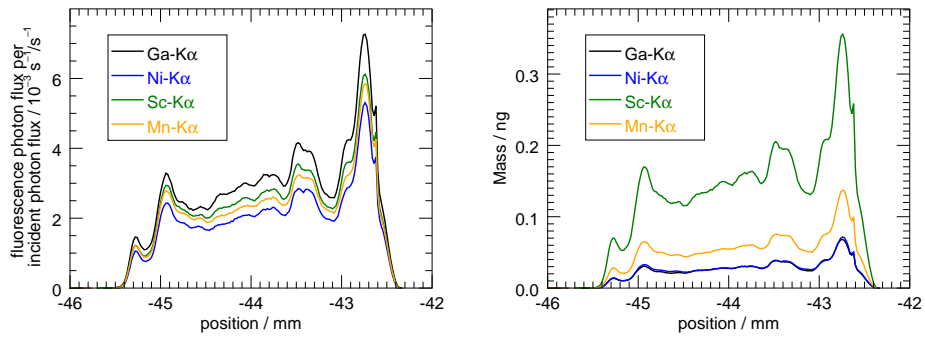
(a) Normalized fluorescence photon flux of the elements Ga, Ni, Mn and Sc from a 50 ng µL droplet sample as a function of the vertical position.

(b) Mass of the µL droplet sample as a function of the vertical position. Modified approaches [11, 12] from Sherman [13] (for the determination of the mass deposition m_i/F_I with the unit area F_I of the element i) were used for a selectable sample size in propagation direction in order to obtain a value of the mass deposition for each element of interest, multiplied by the same preselected sample size and the step size of the lateral scan in vertical direction.

Figure 3: Vertical distribution of the normalized fluorescence photon flux and the respective mass.
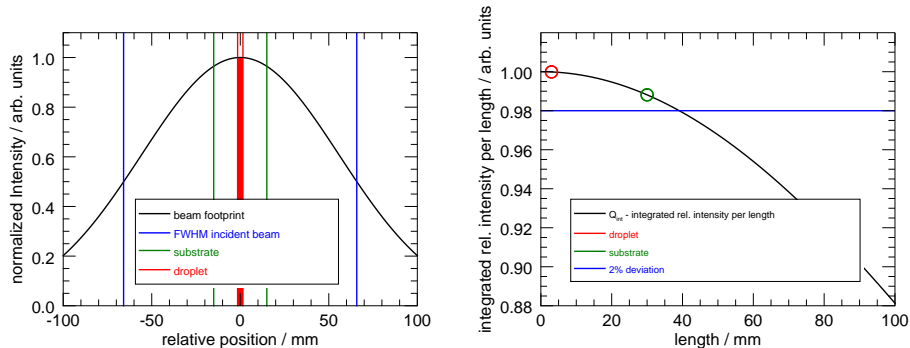
(a) Footprint in propagation direction of the exciting beam for an incident angle of 0.1175° and a respective beam size of 270 µm FWHM. In red, the part of the footprint covering the droplet sample is shown. The green lines indicate the size of the substrate, the blue lines show the position of the FWHM.

(b) Dependence of the length-normalized excitation intensity fraction Q_{int} (equation 2) on the preselected length l. The red and green circle indicates the Quotient Q_{int} for a length of 3 mm (sample) and 30 mm (substrate), respectively. The blue line indicates the 2 % variation at about 40 mm length.

Figure 4: Propagation footprint of the exciting beam and Quotient Q_{int}

The step size of the vertical lateral scan has to be smaller than the vertical beam size in order to ensure that the whole material of the µL droplet is excited. Here, the step size was chosen to be 20 µm. The resulting overlap of the excitation is considered by a numerical integration in the vertical direction for the reference-free quantification.

C Footprint impact on the reference-free quantification

The footprint of the incident beam is larger than the size of the sample in the direction of the propagation of the beam, which ensures an excitation of the whole material in this direction for every vertical position, shown in Figure 4a with an ideal Gaussian distribution as an example. In this case, reference-free TXRF has the advantage to be nearly independent from the information of the precise knowledge of the sample size in the direction of the beam propagation, explained in the following:

Due to the very small incident angle, the quotient Q_{int} of part of the total excitation intensity over a preselectable projected length l (equation 1) normalized to the same length l (equation 2) is almost constant over a large range. Descriptively, Q_{int} is the quotient of the illuminated area and the solid angle of detection defined by this area. This quantity varies by less than 2 % below a length value of 40 mm, which is more than the size of the quartz glass substrate

of all samples used in the Round Robin activity. In practice, this theoretical maximum value for preselected length is further reduced (here to about $8\,mm$) in view of the effective solid angle of detection constraints defined by the detector diameter and angular acceptance [11].

The limit of Q_{int} towards zero is a constant. Due to the normalization of the Gaussian distribution to the maximum value, this constant is equal one. For the uncertainty budget, one may use the maximum Q_{int} deviation of $2\,\%$ as a conservative estimate, assigned to the fraction of the incident beam intensity used for the determination of the mass deposition.

$$I_{0,partial} = \int\limits_{-l/2}^{l/2} P_0 dx \tag{1}$$

$$Q_{int} = \frac{I_{0,partial}}{l} \approx const \tag{2}$$

With further increase of the length, the integral intensity of the beam footprint is reaching the total excitation intensity and the quotient is decreasing. In Figure 4b, this quotient Q_{int} is shown as a function of the length l for a horizontal beam size of $270\,\mu m$ FWHM, an incident angle of $0.1175°$ and a respective footprint of about $130\,mm$ FWHM in propagation direction. For a correct quantification, it is crucial that this chosen length is within the almost constant range of the quotient, but the precise length of the sample does not have to be known.

Here, a length of $3\,mm$ has been chosen for the quantification, being close to the actual size of the µL droplet and sufficiently apart from the two limitations described above. Note that the chosen length (equivalent to preselected sample size) directly has an effect on the fraction of the incident photon flux used for the determination of the mass deposition, but the mass in Figure 3b is almost independent on the chosen length. It gets canceled out when multiplying the mass deposition (determined with the chosen length) and the chosen length itself.

D   Barplots

Shown in barplots are the results of the different droplets and thin film samples from each laboratory for the respective elements. The uncertainty budget has three contributions, the statistical uncertainty of independent measurements, the uncertainty of the internal standard and an estimation of the uncertainty of the instrumentation. Variations in the total uncertainty are due to different statistical uncertainties of the measurements.

D.1   µL droplets barplots

7
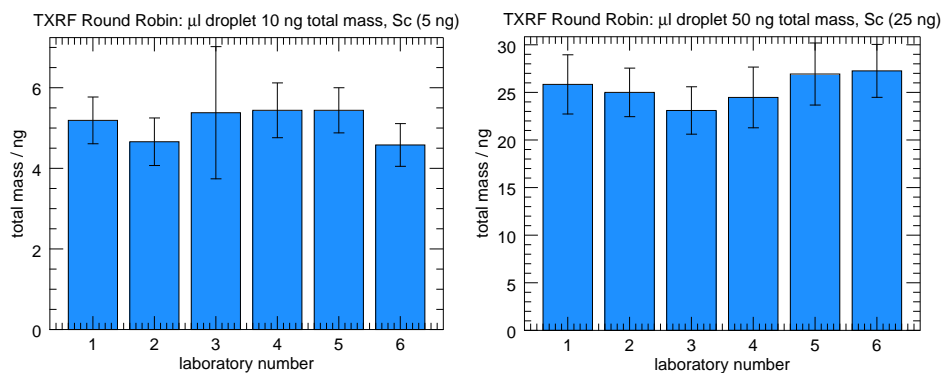
Figure 5: Results of the µL droplets from the respective laboratories for Sc, 10 ng and 50 ng total mass.
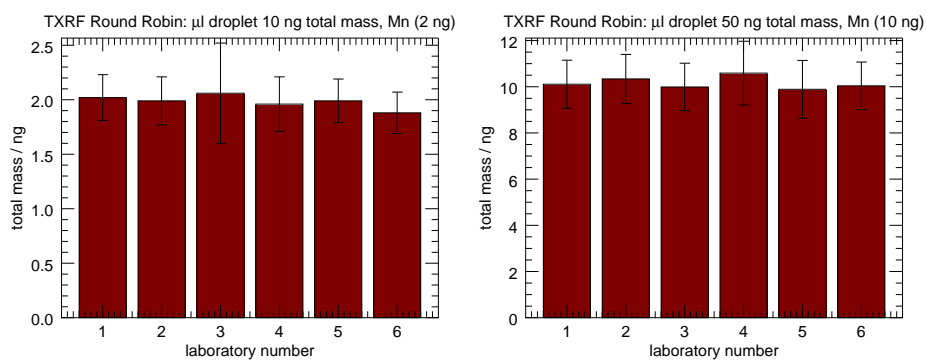
Figure 6: Results of the µL droplets from the respective laboratories for Mn, 10 ng and 50 ng total mass.
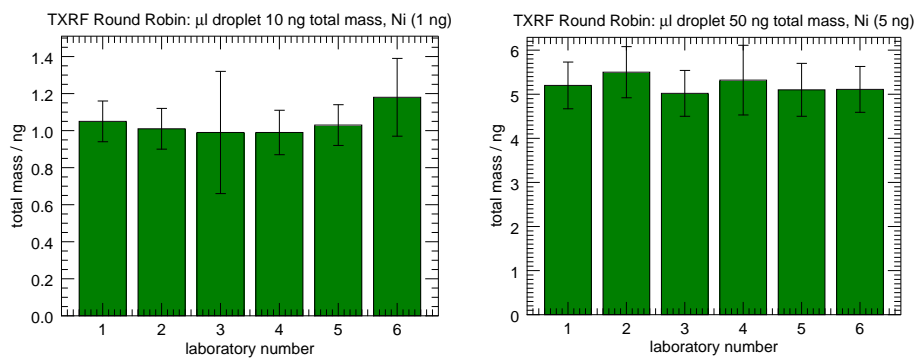
Figure 7: Results of the µL droplets from the respective laboratories for Ni, 10 ng and 50 ng total mass.
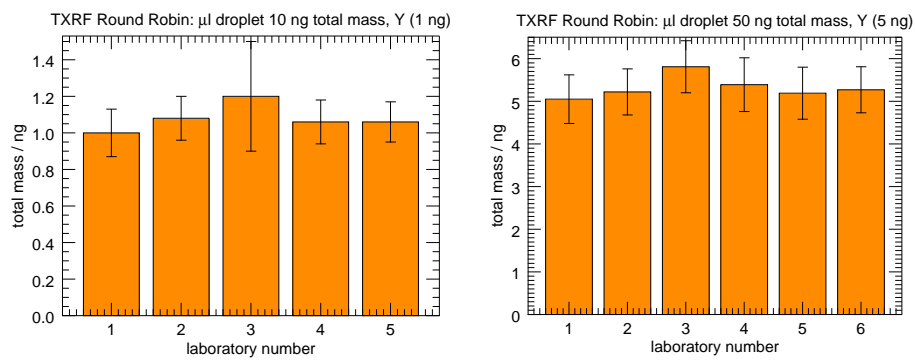
Figure 8: Results of the µL droplets from the respective laboratories for Y, 10 ng and 50 ng total mass.

D.2 nL droplets barplots
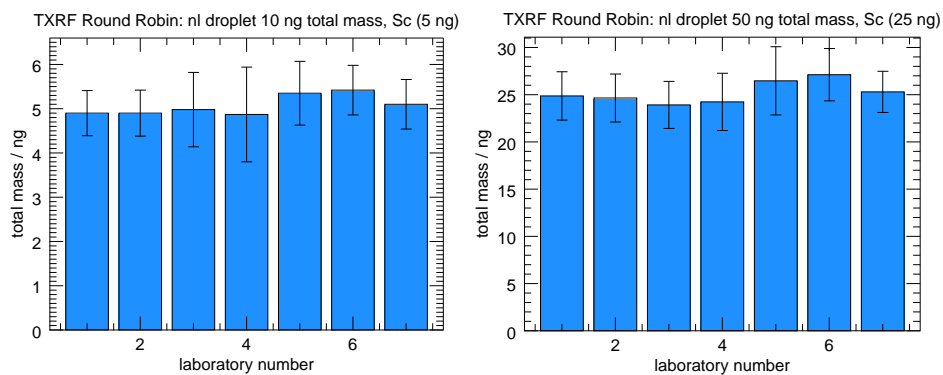
Figure 9: Results of the nL droplets from the respective laboratories for Sc, 10 ng and 50 ng total mass.
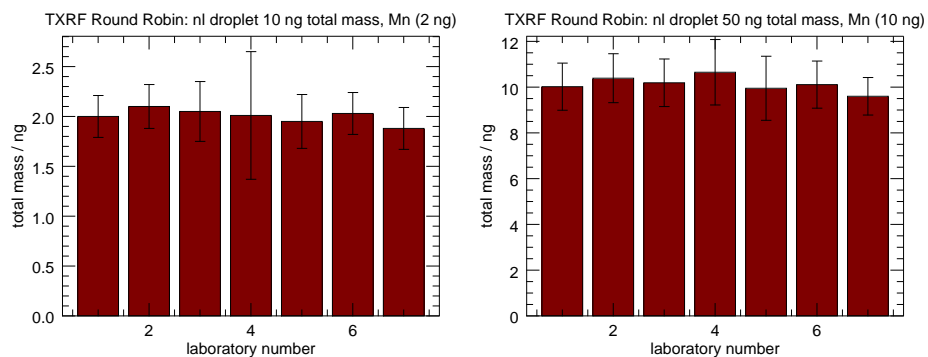
Figure 10: Results of the nL droplets from the respective laboratories for Mn, 10 ng and 50 ng total mass.
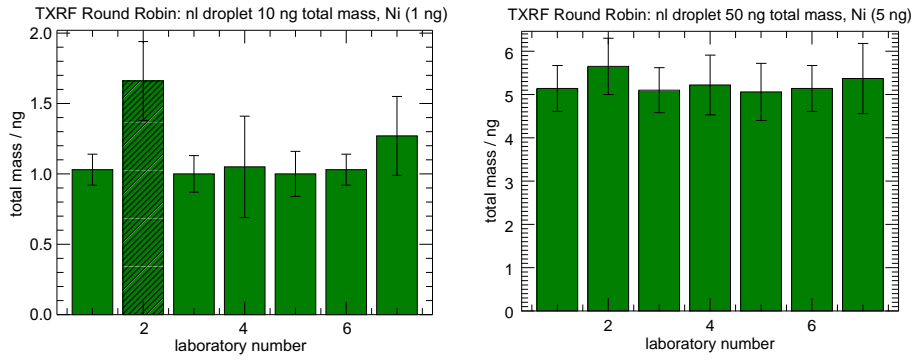
Figure 11: Results of the nL droplets from the respective laboratories for Ni, 10 ng and 50 ng total mass. The bar with stripes indicates a suspected outlier.
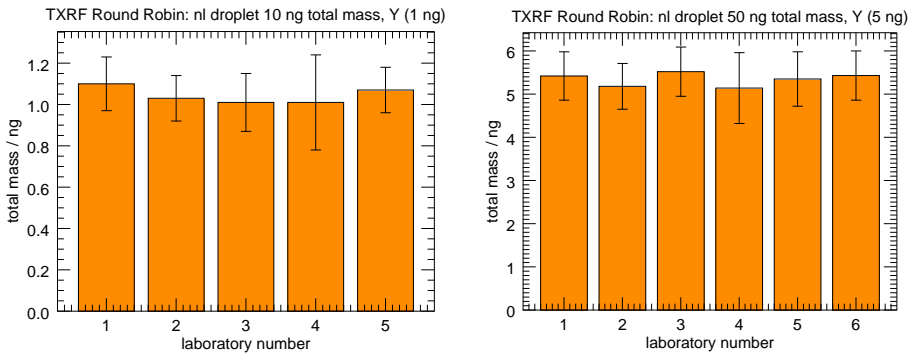
Figure 12: Results of the nL droplets from the respective laboratories for Y, 10 ng and 50 ng total mass.

D.3   Thin film barplots
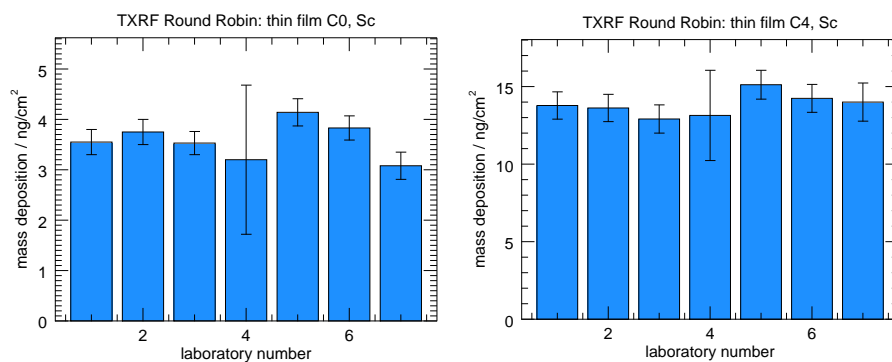
Figure 13: Results of the thin films from the respective laboratories for Sc, C0 and C4
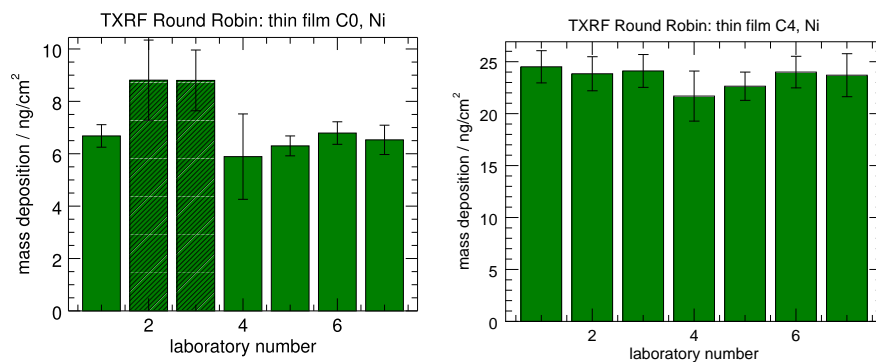
Figure 14: Results of the thin films from the respective laboratories for Ni, C0 and C4. The bars with stripes indicate suspected outliers.

E Boxplots

Before the box plots of all measurements are shown, a principal comparison between a boxplot and a probability density function of a Normal distribution is shown in Figure 15 [14].50 % of all results are located in the range of Q_l and Q_u.
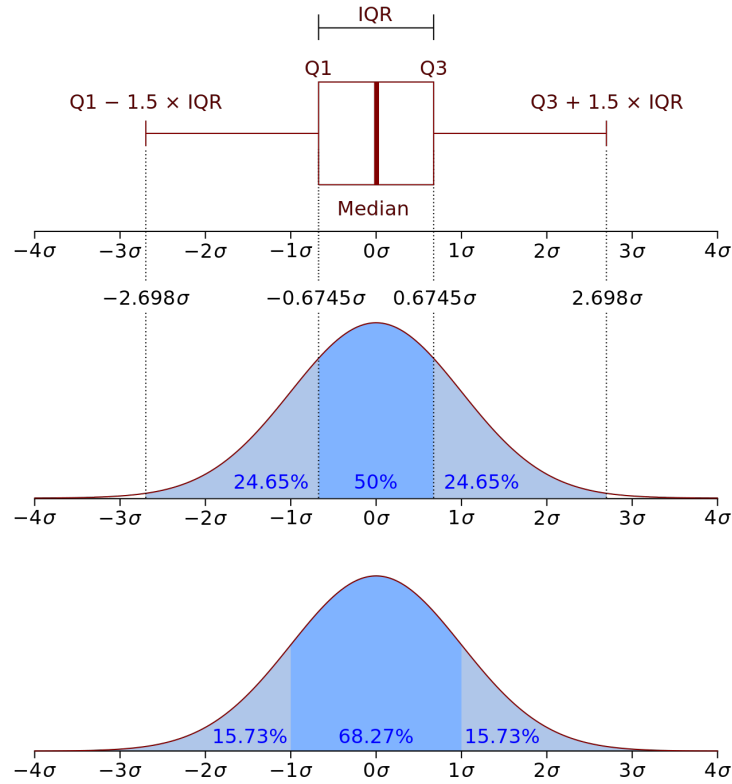
Figure 15: Boxplot and a probability density function of a Normal distribution [14]. Q_1 and Q_3 are similar to Q_l and Q_u, respectively.

E.1 µL droplets boxplots

13
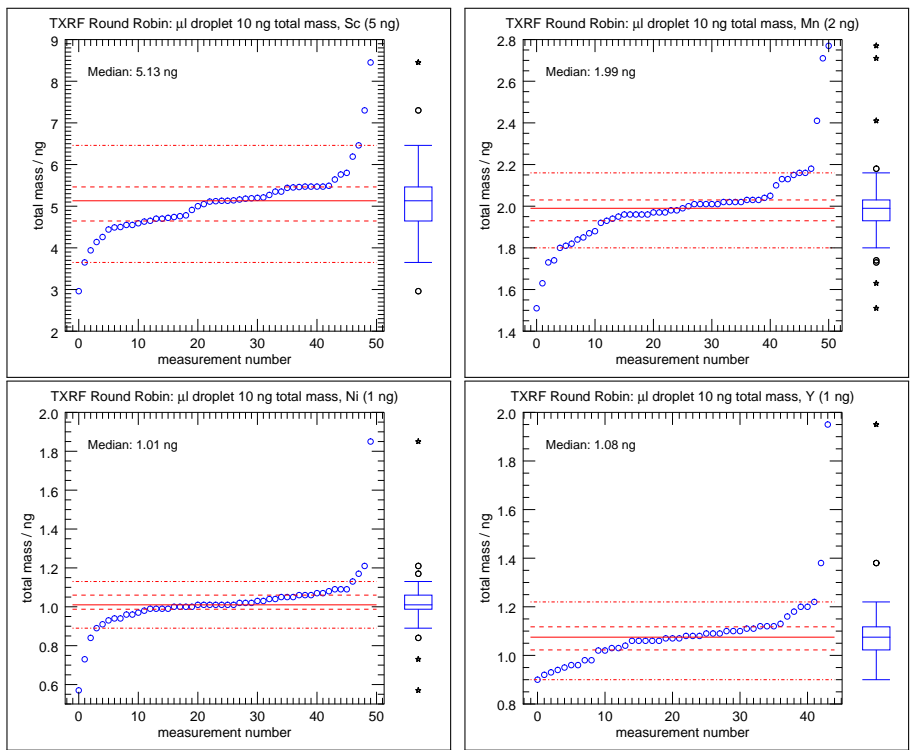
Figure 16: Boxplots of all data points from the measurement of the µL droplets (10 ng total mass). The elements Sc, Mn, Ni and Y are shown.
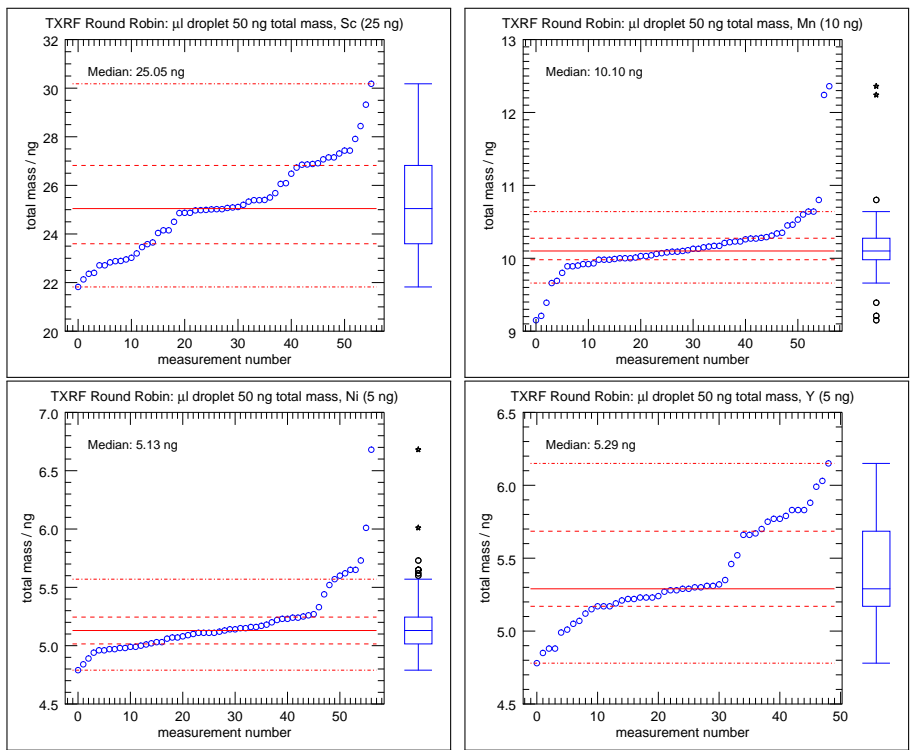
Figure 17: Boxplots of all data points from the measurement of the µL droplets (50 ng total mass). The elements Sc, Mn, Ni and Y are shown.

15

E.2 nL droplets boxplots
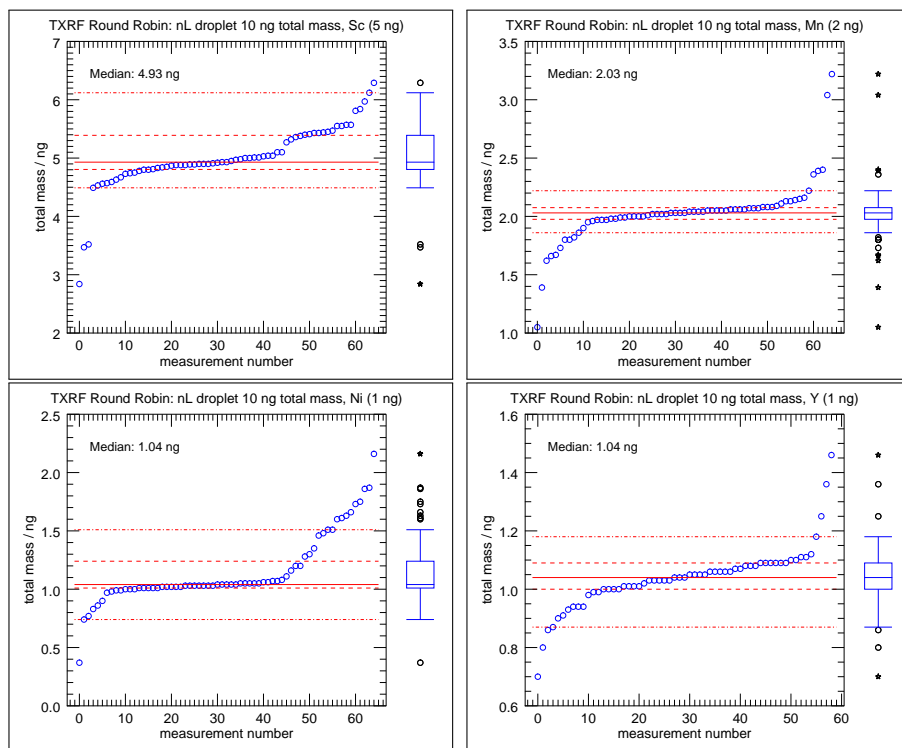
Figure 18: Boxplots of all data points from the measurement of the nL droplets (10 ng total mass). The elements Sc, Mn, Ni and Y are shown.
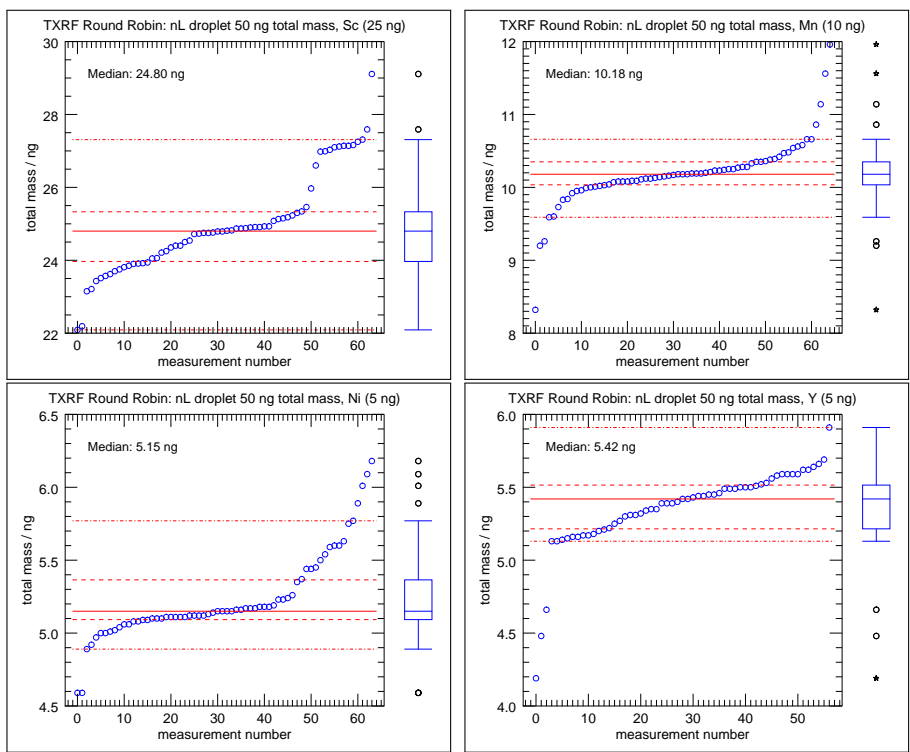
Figure 19: Boxplots of all data points from the measurement of the nL droplets (50 ng total mass). The elements Sc, Mn, Ni and Y are shown.

E.3   Thin film boxplots
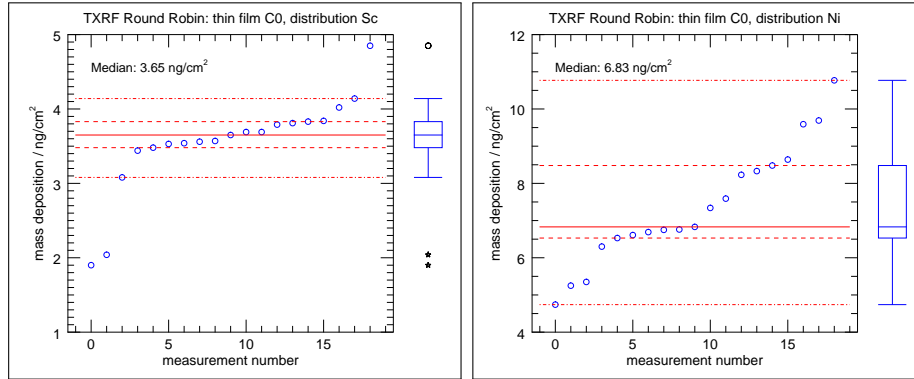
Figure 20: Boxplots of all data points from the measurement of the thin film C0 sample. The elements Sc and Ni are shown.
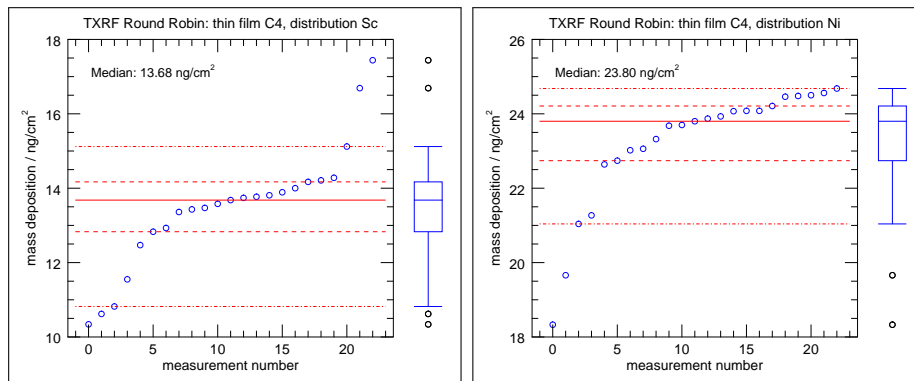
Figure 21: Boxplots of all data points from the measurement of the thin film C4 sample. The elements Sc and Ni are shown.

F   Uncertainty budgets

In the following tables, the uncertainty budgets for the reference-free TXRF quantification of the Sc, Mn, Ni and Ga are listed, calculated with the GUM Workbench [15]. The element-specific mass within the dried-in droplet was determined at one vertical lateral position. For the fraction of the incident beam in propagation direction (defined by the chosen integration length of 3 mm, i.e. the preselected sample size) $P_{0,frac}$, an uncertainty of 2 % was estimated. The uncertainty contribution of the numerical integration in both directions is negligible for the uncertainty of the total mass.

18

According to GUM, the uncertainty index $h(x_i)$ for non-correlated quantities is defined as follows:

$$h(x_i) = \frac{u_i^2}{u^2} \tag{3}$$

Here, x_i is the input quantity, u is the total uncertainty and u_i is the uncertainty contribution of the input quantity. The uncertainty contribution u_i is the product of the standard uncertainty $u(x_i)$ and the sensitivity coefficient c_i of the respective input quantity. The sensitivity coefficient c_i can become negative. From this it follows that the uncertainty contribution u_i can become negative as well.

$$u_i = c_i \cdot u(x_i) \tag{4}$$

quantity	value	standard uncertainty	uncertainty contribution / pg	uncertainty index / %
μ_{E_0}	$89.13\,\mathrm{cm^2\,g^{-1}}$	$1.78\,\mathrm{cm^2\,g^{-1}}$ [16]	0.015	0.0
μ_{E_i}	$127.34\,\mathrm{cm^2\,g^{-1}}$	$6.37\,\mathrm{cm^2\,g^{-1}}$ [16]	1.1×10^{-4}	0.0
μ_{tot,E_0,E_i}	$43\,589\,\mathrm{cm^2\,g^{-1}}$	$889\,\mathrm{cm^2\,g^{-1}}$		
Ψ_{in}	$0.1175°$	$5 \times 10^{-4}°$ [17]	0.62	0.0
$\omega_{K_{Sc}}$	0.1962	0.0148 [18]	-11	11.1
$g_{K_\alpha,K_{Sc}}$	0.8848	2.04×10^{-3} [19]	0.34	0.0
Ω_{det}	$1.2434 \times 10^{-3}\,\mathrm{sr}$	$4.97 \times 10^{-5}\,\mathrm{sr}$ [11]	-5.9	3.1
I_{XSW}	1.6	≤ 0.32	-30	83.4
τ_{K_{Sc},E_0}	$77.63\,\mathrm{cm^2\,g^{-1}}$	$1.55\,\mathrm{cm^2\,g^{-1}}$ [16]	-2.9	0.8
S_0	$7.348\,728 \times 10^{-7}\,\mathrm{A}$	$7.35 \times 10^{-11}\,\mathrm{A}$ [20]	-0.015	0.0
σ_{diode,E_0}	$0.2354\,\mathrm{A\,W^{-1}}$	$2.35 \times 10^{-3}\,\mathrm{A\,W^{-1}}$ [20]	1.5	0.2
E_0	$10.5\,\mathrm{keV}$	$1.05\,\mathrm{eV}$ [8]	0.015	0.0
P_0	$1.8557 \times 10^9\,\mathrm{s^{-1}}$	$1.86 \times 10^7\,\mathrm{s^{-1}}$		
$P_{0,frac}$	1.00	≤ 0.02	-2.9	0.8
$counts_{Sc}$	29\,510	172	0.85	0.0
$lifetime$	$63.4\,\mathrm{s}$	$\leq 0.6\,\mathrm{s}$	-1.4	0.2
R_{Sc}	$465.37\,\mathrm{s^{-1}}$	$5.17\,\mathrm{s^{-1}}$		
ε_{det,E_i}	1.000	0.015 [21]	-2.2	0.4
P_{Sc}	$465.37\,\mathrm{s^{-1}}$	$8.69\,\mathrm{s^{-1}}$		
dx	$0.002\,\mathrm{cm}$			
$length_y$	$0.3\,\mathrm{cm}$			
$m_{Sc,x}$	$145.4\,\mathrm{pg}$	$33.4\,\mathrm{pg}$		
total mass $_{Sc}$	$22.07\,\mathrm{ng}$	$5.05\,\mathrm{ng}$		

Table 1: Uncertainty budget for the reference-free TXRF quantification of Sc at one exemplary vertical lateral position x (here: $-44.0\,\mathrm{mm}$, see Figure 3b) and for the total mass of Sc. The standard uncertainties with the symbol $\leq$ are estimated. d_x is the step width of the vertical scan and $length_y$ is the integration length (preselected sample size) in propagation direction of the beam.

quantity	value	standard uncertainty	uncertainty contribution / pg	uncertainty index / %
μ_{E_0}	$133.09\,\mathrm{cm^2\,g^{-1}}$	$2.66\,\mathrm{cm^2\,g^{-1}}$ [16]	3.3×10^{-3}	0.0
μ_{E_i}	$74.24\,\mathrm{cm^2\,g^{-1}}$	$1.48\,\mathrm{cm^2\,g^{-1}}$ [16]	3.8×10^{-6}	0.0
μ_{tot,E_0,E_i}	$64\,970\,\mathrm{cm^2\,g^{-1}}$	$1330\,\mathrm{cm^2\,g^{-1}}$		
Ψ_{in}	$0.1175°$	$5 \times 10^{-4}°$ [17]	0.23	0.0
$\omega_{K_{Mn}}$	0.321	0.012 [18]	-4.2	10.9
$g_{K_\alpha,K_{Mn}}$	0.881 83	3.11×10^{-3} [22]	0.32	0.0
Ω_{det}	$1.2434 \times 10^{-3}\,\mathrm{sr}$	$4.97 \times 10^{-5}\,\mathrm{sr}$ [11]	-2.2	3.1
I_{XSW}	1.6	≤ 0.32	-11	83.6
τ_{K_{Mn},E_0}	$117.41\,\mathrm{cm^2\,g^{-1}}$	$2.35\,\mathrm{cm^2\,g^{-1}}$ [16]	-1.1	0.8
S_0	$7.348\,728 \times 10^{-7}\,\mathrm{A}$	$7.35 \times 10^{-11}\,\mathrm{A}$ [20]	-5.5×10^{-3}	0.0
σ_{diode,E_0}	$0.2354\,\mathrm{A\,W^{-1}}$	$2.35 \times 10^{-3}\,\mathrm{A\,W^{-1}}$ [20]	0.55	0.2
E_0	$10.5\,\mathrm{keV}$	$1.05\,\mathrm{eV}$ [8]	5.5×10^{-3}	0.0
P_0	$1.8557 \times 10^9\,\mathrm{s^{-1}}$	$1.86 \times 10^7\,\mathrm{s^{-1}}$		
$P_{0,frac}$	1.00	≤ 0.02	-1.1	0.8
$counts_{Mn}$	27 339	165	0.33	0.0
$lifetime$	$63.4\,\mathrm{s}$	$\leq 0.6\,\mathrm{s}$	-0.52	0.2
R_{Mn}	$431.14\,\mathrm{s^{-1}}$	$4.84\,\mathrm{s^{-1}}$		
ε_{det,E_i}	1.000	0.015 [21]	-0.83	0.4
P_{Mn}	$431.14\,\mathrm{s^{-1}}$	$8.08\,\mathrm{s^{-1}}$		
dx	$0.002\,\mathrm{cm}$			
$length_y$	$0.3\,\mathrm{cm}$			
$m_{Mn,x}$	$54.4\,\mathrm{pg}$	$12.4\,\mathrm{pg}$		
total mass $_{Mn}$	$8.32\,\mathrm{ng}$	$1.97\,\mathrm{ng}$		

Table 2: Uncertainty budget for the reference-free TXRF quantification of Mn at one exemplary vertical lateral position x (here: $-44.0\,\mathrm{mm}$, see Figure 3b) and for the total mass of Mn. The standard uncertainties with the symbol $\leq$ are estimated. d_x is the step width of the vertical scan and $length_y$ is the integration length (preselected sample size) in propagation direction of the beam.

quantity	value	standard uncertainty	uncertainty contribution / pg	uncertainty index / %
μ_{E_0}	183.96 cm² g⁻¹	3.68 cm² g⁻¹ [23]	1.1×10^{-3}	0.0
μ_{E_i}	57.68 cm² g⁻¹	1.15 cm² g⁻¹ [23]	0.73×10^{-6}	0.0
μ_{tot,E_0,E_i}	89 760 cm² g⁻¹	1830 cm² g⁻¹		
Ψ_{in}	0.1175°	5×10^{-4}° [17]	0.12	0.0
$\omega_{K_{Ni}}$	0.410	0.014 [23]	−0.94	2.5
$g_{K_\alpha,K_{Ni}}$	0.8834	4.7×10^{-3} [23]	0.15	0.0
Ω_{det}	1.2434×10^{-3} sr	4.97×10^{-5} sr [11]	−1.1	3.4
I_{XSW}	1.6	≤0.32	−5.7	91.4
τ_{K_{Ni},E_0}	160.03 cm² g⁻¹	3.2 cm² g⁻¹ [16]	−0.55	0.8
S_0	$7.348\,728 \times 10^{-7}$ A	7.35×10^{-11} A [20]	-2.8×10^{-3}	0.0
σ_{diode,E_0}	0.2354 A W⁻¹	2.35×10^{-3} A W⁻¹ [20]	0.28	0.2
E_0	10.5 keV	1.05 eV [8]	2.8×10^{-3}	0.0
P_0	1.8557×10^{9} s⁻¹	1.86×10^{7} s⁻¹		
$P_{0,frac}$	1.00	≤0.02	−0.55	0.8
$counts_{Ni}$	24 380	156	0.18	0.0
$lifetime$	63.4 s	≤0.6 s	−0.26	0.2
R_{Ni}	379.50 s⁻¹	4.39 s⁻¹		
ε_{det,E_i}	1.000	0.015 [21]	−0.41	0.5
P_{Ni}	379.50 s⁻¹	7.16 s⁻¹		
dx	0.002 cm			
$length_y$	0.3 cm			
$m_{Ni,x}$	27.48 pg	6.00 pg		
total mass $_{Ni}$	4.21 ng	0.92 ng		

Table 3: Uncertainty budget for the reference-free TXRF quantification of Ni at one exemplary vertical lateral position x (here: -44.0 mm, see Figure 3b) and for the total mass of Ni. The standard uncertainties with the symbol ≤ are estimated. d_x is the step width of the vertical scan and $length_y$ is the integration length (preselected sample size) in propagation direction of the beam.

quantity	value	standard uncertainty	uncertainty contribution / pg	uncertainty index / %
μ_{E_0}	$217.47\,\mathrm{cm^2\,g^{-1}}$	$4.35\,\mathrm{cm^2\,g^{-1}}$ [16]	1.3×10^{-3}	0.0
μ_{E_i}	$40.64\,\mathrm{cm^2\,g^{-1}}$	$0.81\,\mathrm{cm^2\,g^{-1}}$ [16]	0.51×10^{-6}	0.0
μ_{tot,E_0,E_i}	$106\,080\,\mathrm{cm^2\,g^{-1}}$	$2170\,\mathrm{cm^2\,g^{-1}}$		
Ψ_{in}	$0.1175°$	$5 \times 10^{-4}°$ [17]	0.12	0.0
$\omega_{K_{Ga}}$	0.514	0.010 [24]	-0.54	0.8
$g_{K_\alpha,K_{Ga}}$	0.8749	2.2×10^{-3} [19]	0.069	0.0
Ω_{det}	$1.2434 \times 10^{-3}\,\mathrm{sr}$	$4.97 \times 10^{-5}\,\mathrm{sr}$ [11]	-1.1	3.4
I_{XSW}	1.6	≤ 0.32	-5.7	93.0
τ_{K_{Ga},E_0}	$184.55\,\mathrm{cm^2\,g^{-1}}$	$3.69\,\mathrm{cm^2\,g^{-1}}$ [16]	0.55	0.9
S_0	$7.348\,728 \times 10^{-7}\,\mathrm{A}$	$7.35 \times 10^{-11}\,\mathrm{A}$ [20]	-2.7×10^{-3}	0.0
σ_{diode,E_0}	$0.2354\,\mathrm{A\,W^{-1}}$	$2.35 \times 10^{-3}\,\mathrm{A\,W^{-1}}$ [20]	0.27	0.2
E_0	$10.5\,\mathrm{keV}$	$1.05\,\mathrm{eV}$ [8]	2.7×10^{-3}	0.0
P_0	$1.8557 \times 10^{9}\,\mathrm{s^{-1}}$	$1.86 \times 10^{7}\,\mathrm{s^{-1}}$		
$P_{0,frac}$	1.00	≤ 0.02	-0.55	0.9
$counts_{Ga}$	34 241	155	0.15	0.0
$lifetime$	$63.4\,\mathrm{s}$	$\leq 0.6\,\mathrm{s}$	-0.26	0.2
R_{Ga}	$539.98\,\mathrm{s^{-1}}$	$5.88\,\mathrm{s^{-1}}$		
ε_{det,E_i}	0.9989	0.015 [21]	-0.41	0.5
P_{Ga}	$540.6\,\mathrm{s^{-1}}$	$10.0\,\mathrm{s^{-1}}$		
dx	$0.002\,\mathrm{cm}$			
$length_y$	$0.3\,\mathrm{cm}$			
$m_{Ga,x}$	$27.35\,\mathrm{pg}$	$5.92\,\mathrm{pg}$		
total mass $_{Ga}$	$4.12\,\mathrm{ng}$	$0.89\,\mathrm{ng}$		

Table 4: Uncertainty budget for the reference-free TXRF quantification of Ga at one exemplary vertical lateral position x (here: $-44.0\,\mathrm{mm}$, see Figure 3b) and for the total mass of Ga. The standard uncertainties with the symbol $\leq$ are estimated. d_x is the step width of the vertical scan and $length_y$ is the integration length (preselected sample size) in propagation direction of the beam.

References

[1] A. Iida et al. "Grazing incidence X-ray fluorescence analysis". In: *Nuclear Instruments and Methods in Physics Research Section A: Accelerators, Spectrometers, Detectors and Associated Equipment* 246.1 (1986), pp. 736–738. ISSN: 0168-9002. DOI: https://doi.org/10.1016/0168-9002(86)90182-8. URL: http://www.sciencedirect.com/science/article/pii/0168900286901828.

[2] Alex von Bohlen. "Total reflection X-ray fluorescence and grazing incidence X-ray spectrometry – Tools for micro- and surface analysis. A review". In: *Spectrochimica Acta Part B: Atomic Spectroscopy* 64.9 (2009), pp. 821–832. ISSN: 0584-8547. DOI: https://doi.org/10.1016/j.sab.2009.06.012.

[3] "Performance of TXRF and GI-XRF Analyses". In: *Total-Reflection X-Ray Fluorescence Analysis and Related Methods*. John Wiley & Sons, Ltd, 2014. Chap. 4, pp. 205–290. ISBN: 9781118460276. DOI: 10.1002/9781118985953.ch04. eprint: https://onlinelibrary.wiley.com/doi/pdf/10.1002/9781118985953.ch04. URL: https://onlinelibrary.wiley.com/doi/abs/10.1002/9781118985953.ch04.

[4] Markus Krämer et al. "X-ray standing waves: a method for thin layered systems". In: *J. Anal. At. Spectrom.* 21 (11 2006), pp. 1136–1142. DOI: 10.1039/B607252F. URL: http://dx.doi.org/10.1039/B607252F.

[5] M. Krämer et al. "Synchrotron radiation induced X-ray standing waves analysis of layered structures". In: *Applied Surface Science* 253.7 (2007), pp. 3533–3542. ISSN: 0169-4332. DOI: https://doi.org/10.1016/j.apsusc.2006.07.076. URL: http://www.sciencedirect.com/science/article/pii/S0169433206010208.

[6] "Principles of Total Reflection XRF". In: *Total-Reflection X-Ray Fluorescence Analysis and Related Methods*. John Wiley & Sons, Ltd, 2014. Chap. 2, pp. 79–125. ISBN: 9781118460276. DOI: 10.1002/9781118985953.ch02. eprint: https://onlinelibrary.wiley.com/doi/pdf/10.1002/9781118985953.ch02. URL: https://onlinelibrary.wiley.com/doi/abs/10.1002/9781118985953.ch02.

[7] Norbert Streckfuß. *Charakterisierung von Siliciumoberflächen mittels Röntgenfluoreszenzanalyse unter Totalreflexionsbedingungen*. PhD Thesis. Erlangen 1995.

[8] M. Krumrey. "Design of a Four-Crystal Monochromator Beamline for Radiometry at BESSY II". In: *Journal of Synchrotron Radiation* 5.1 (Jan. 1998), pp. 6–9. DOI: 10.1107/S0909049597011825. URL: https://doi.org/10.1107/S0909049597011825.

[9] J. Magnes et al. "Quantitative and Qualitative Study of Gaussian Beam Visualization Techniques". In: *ArXiv Physics e-prints* (May 2006). eprint: arXiv:physics/0605102.

[10] R. Unterumsberger et al. "Focusing of soft X-ray radiation and characterization of the beam profile enabling X-ray emission spectrometry at nanolayered specimens". In: *Spectrochimica Acta Part B: Atomic Spectroscopy* 78 (2012), pp. 37–41. ISSN: 0584-8547. DOI: `https://doi.org/10.1016/j.sab.2012.10.001`. URL: `http://www.sciencedirect.com/science/article/pii/S0584854712003400`.

[11] Burkhard Beckhoff et al. "Reference-free total reflection X-ray fluorescence analysis of semiconductor surfaces with synchrotron radiation". In: *Analytical chemistry* 79.20 (2007), pp. 7873–7882.

[12] Rainer Unterumsberger et al. "Complementary Characterization of Buried Nanolayers by Quantitative X-ray Fluorescence Spectrometry under Conventional and Grazing Incidence Conditions". In: *Analytical Chemistry* 83.22 (2011). PMID: 21961904, pp. 8623–8628. DOI: `10.1021/ac202074s`.

[13] Jacob Sherman. "The theoretical derivation of fluorescent X-ray intensities from mixtures". In: *Spectrochimica Acta* 7 (1955), pp. 283–306. ISSN: 0371-1951. DOI: `10.1016/0371-1951(55)80041-0`.

[14] Wikimedia Commons. *Boxplot and a probability density function (pdf) of a Normal N(0,1σ2) Population*. Mar. 2011. URL: `https://upload.wikimedia.org/wikipedia/commons/1/1a/Boxplot_vs_PDF.svg`.

[15] *GUM Workbench*. Version 2.4.1.392. Metrodata GmbH. 1996-2010.

[16] John H. Hubbell. "Compilation of photon cross-sections: some historical remarks and current status". In: *X-Ray Spectrometry* 28.4 (1999), pp. 215–223. DOI: `10.1002/(SICI)1097-4539(199907/08)28:4<215::AID-XRS336>3.0.CO;2-5`. eprint: `https://onlinelibrary.wiley.com/doi/pdf/10.1002/%28SICI%291097-4539%28199907/08%2928%3A4%3C215%3A%3AAID-XRS336%3E3.0.CO%3B2-5`. URL: `https://onlinelibrary.wiley.com/doi/abs/10.1002/%28SICI%291097-4539%28199907/08%2928%3A4%3C215%3A%3AAID-XRS336%3E3.0.CO%3B2-5`.

[17] Janin Lubeck et al. "A novel instrument for quantitative nanoanalytics involving complementary X-ray methodologies." In: *Review of Scientific Instruments* 84.4 (2013), p. 045106.

[18] W. Bambynek. "A New Evaluation of K -Shell Fluorescence Yields (Fit: K: $5 \leq Z \leq 100$)". In: *Proc. Int. Conf. on X-Ray and Inner-Shell Processes in Atoms, Molecules and Solids* 66.11 (1984), pp. 776–784.

[19] S. I. Salem, T. H. Falconer, and R. W. Winchell. "$\frac{K\beta}{K\alpha}$ Radiative-Transition-Probability Ratios for Elements of Low Atomic Numbers in Amorphous and Crystal Forms". In: *Phys. Rev. A* 6 (6 Dec. 1972), pp. 2147–2150. DOI: `10.1103/PhysRevA.6.2147`. URL: `https://link.aps.org/doi/10.1103/PhysRevA.6.2147`.

[20] Michael Krumrey and Gerhard Ulm. "High-accuracy detector calibration at the PTB four-crystal monochromator beamline". In: *Nuclear Instruments and Methods in Physics Research. Section A, Accelerators, Spectrometers, Detectors and Associated Equipment* 467-468 (1 July 2001). DOI: `10.1016/S0168-9002(01)00598-8`.

[21] Frank Scholze and M. Procop. "Modelling the response function of energy dispersive X-ray spectrometers with silicon detectors". In: *X-Ray Spectrometry* 38.4 (2009), pp. 312–321. DOI: `10.1002/xrs.1165`. eprint: `https://onlinelibrary.wiley.com/doi/pdf/10.1002/xrs.1165`. URL: `https://onlinelibrary.wiley.com/doi/abs/10.1002/xrs.1165`.

[22] P. Jonnard, G. Giorgi, and C. Bonnelle. "Experimental and theoretical K x-ray spectra of manganese". In: *Phys. Rev. A* 65 (3 Feb. 2002), p. 032507. DOI: `10.1103/PhysRevA.65.032507`. URL: `https://link.aps.org/doi/10.1103/PhysRevA.65.032507`.

[23] Y Ménesguen et al. "Experimental determination of the x-ray atomic fundamental parameters of nickel". In: *Metrologia* 55.1 (Dec. 2017), pp. 56–66. DOI: `10.1088/1681-7575/aa9b12`. URL: `https://doi.org/10.1088%2F1681-7575%2Faa9b12`.

[24] Rainer Unterumsberger et al. "Accurate experimental determination of gallium K- and L3-shell XRF fundamental parameters". In: *J. Anal. At. Spectrom.* 33 (6 2018), pp. 1003–1013. DOI: `10.1039/C8JA00046H`. URL: `http://dx.doi.org/10.1039/C8JA00046H`.